MNRAS **000**, 1–?? (2002) Preprint 25 November 2015 Compiled using MNRAS LaTeX style file v3.0

HELP: XID+, The Probabilistic De-blender for *Herschel* SPIRE maps

P.D. Hurley,[1⋆] S. Oliver,[1] J.M. Scudder,[1] M. Griffin,[2] S. Duivenvoorden,[1] M. Sargent,[1] L. Wang[3]

[1] *Astronomy Centre, Department of Physics and Astronomy, University of Sussex, Falmer, Brighton BN1 9QH, UK*
[2] *Cardiff School of Physics and Astronomy, Cardiff University, Queens Buildings, The Parade, Cardiff CF24 3AA*
[3] *SRON Netherlands Institute for Space Research, Landleven 12, 9747 AD, Groningen, The Netherlands*

Released 2002 Xxxxx XX

ABSTRACT
As part of the *Herschel* Extragalactic Legacy Project (HELP), we have developed a new prior based source extraction tool, XID+, to carry out prior source extraction on the *Herschel* SPIRE maps covered by HELP. XID+ is developed using a probabilistic Bayesian framework which provides a natural framework in which to introduce prior information, and uses the Bayesian inference tool *Stan* to obtain the full posterior probability distribution on flux estimates. In this paper, we discuss the details of XID+ and demonstrate the basic capabilities and performance by running it on simulated SPIRE maps resembling the COSMOS field, and comparing to the current prior based source extraction tool DESPHOT. We show that not only does XID+ perform better on metrics such as flux accuracy and flux uncertainty accuracy, we illustrate how obtaining the posterior probability distribution can help overcome some of the inherent issues associated with maximum likelihood based source extraction routines. We run XID+ on the COSMOS SPIRE maps from HerMES, using a 24 μm catalogue as a prior and show the marginalised SPIRE colour-colour plot and marginalised contribution to the cosmic infrared background at the SPIRE wavelengths. For the first time, we provide the posterior probability samples for the COSMOS field as a data product, alongside the more standard catalogue. We also discuss how additional work within HELP on providing prior information on fluxes can and will be utilised by XID+. Software available at https://github.com/pdh21/XID_plus/.

Key words: galaxies: statistics – infrared: galaxies

1 INTRODUCTION

Ever since the discovery of the far-infrared background by the *Cosmic Background Explorer* COBE; (Puget et al. 1996), surveys have aimed to observe and detect the sources responsible. Most of those sources are galaxies, with the far-infrared emission coming from dust.

While ground-based observatories such as SCUBA (Holland et al. 1999), and more recently SCUBA-2 (Holland et al. 2013) and ALMA can make use of infrared atmospheric transmission windows to observe at the tail of the cosmic infrared background, only space-borne facilities can observe at the peak. The first infrared space telescope, the InfraRed Astronomical Satellite (IRAS; Neugebauer et al. (1984)), observed the whole sky in four bands centred at 12, 25, 60 and 100 μm and revealed new populations of galaxies which were optically faint but luminous in the infrared (Soifer et al. 1984).

While the Infrared Space Observatory, ISO; Kessler et al. (1996) and the Spitzer Space Telescope (Werner et al. 2004) have provided deep near and mid-infrared photometry over small fields, other smaller space-borne facilities such as AKARI (Murakami et al. 2007) and the Wide-field Infrared Survey Explorer, WISE; Wright et al. (2010) have surveyed the entire sky at mid to far-infrared and near to mid infrared wavelengths respectively. The most recent advance in infrared astronomy has been made with the ESA *Herschel* Space Observatory (Pilbratt et al. 2010). Photometry from the Photoconductor Array Camera and Spectrometer (PACS; Poglitsch et al. 2010) and Spectral and Photometric Imaging Receiver (SPIRE; Griffin et al. 2010) have given us an unprecedented view of the far-infrared Universe by providing observations that measure across the peak of the far-infrared background and at greater sensitivity and resolution than has been achieved previously at these wavelengths.

⋆ Email: p.d.hurley@sussex.ac.uk

With surveys such as the *Herschel* Multi-Tiered Extragalactic Survey, HerMES; Oliver et al. (2012) and the *Herschel* ATLAS survey, H-ATLAS; Eales et al. (2010), over 1000 square degrees of the sky has been observed by the SPIRE instrument. However, due to the relatively large beam size of the SPIRE, and the galaxy density (≈ 30 per SPIRE beam for optical sources with $B < 28$), multiple galaxies can be located within the SPIRE beam. This is referred to as the problem of source confusion,

To obtain accurate photometry from the SPIRE maps, overcoming the source confusion problem is essential. One way to solve the problem is to use prior information to accurately distribute the flux in the SPIRE maps to the underlying astronomical objects. For example, if we know the location of a galaxy to a reasonable tolerance (e.g. from an optical image where resolution is better), we may expect a galaxy to be found in the SPIRE maps at the same location.

Several techniques have been developed that utilise the positions of sources detected at other wavelengths, usually 24 μm and 1.4 GHz, to disentangle the various contributions from discrete sources to the SPIRE flux in a given beam element (e.g. Roseboom et al. 2010, 2011; Chapin et al. 2011). This process is made possible by the strong correlation between the 24-μm and 1.4-GHz populations and those observed at far-IR wavelengths; >80 per cent of the cosmic IR background at SPIRE wavelengths can be accounted for by 24-μm sources with $S24 > 25$ μJy (e.g. Marsden et al. 2009; Pascale et al. 2009; Elbaz et al. 2010; Béthermin et al. 2012), while the strong correlation between the far-IR and radio luminosity is known to hold across a wide range in redshift and luminosity (e.g. Ivison et al. 2010). Up to the present day, most of these techniques have used a maximum likelihood optimisation approach, which suffers from two major issues. The first is that variance and co-variance of source fluxes can not be properly estimated. The second is that of overfitting when many of the input sources are intrinsically faint. The list driven algorithm developed for HerMES (DESPHOT Roseboom et al. 2011; Wang et al. 2014) tried to overcome this by using the non-negative weighted LASSO algorithm (Tibshirani 1996; Zou 2006; ter Braak et al. 2010), a shrinkage and selection method which introduces an additional penalty term in an attempt to reduce the number of sources needed to fit the map. However, when multiple sources are located close-by (i.e. within the SPIRE beam), the method has been found to wrongly assign all the flux to one source.

The solution to both of these problems is to fully explore the posterior probability distribution with Bayesian inference techniques such as Markov Chain Monte Carlo (MCMC) methods. By fully exploring the posterior, the variance and covariance between sources can be properly estimated. Also, by considering the covariance between sources (i.e. how the flux of sources affect each other), the probability of sources being very faint or bright is taken into account, removing the need for methods such as LASSO.

Up until the present day, use of MCMC techniques has been computationally unfeasible. However, advances in computational technology and algorithms such as Hamiltonian Monte Carlo now make this sort of approach a viable alternative, as demonstrated by Safarzadeh et al. (2015), who used an MCMC based approach to fit PACS simulated maps.

As part of the *Herschel Extragalactic Legacy Project* (HELP; Oliver in prep.), we have developed an alternative prior based approach for source extraction in confusion-dominated maps. Our new method, XID+, is built upon a Bayesian probabilistic framework which provides a natural way in which to introduce additional prior information. By using the Bayesian inference tool, (*Stan* Stan Development Team 2015a,b) to sample the full posterior distribution, we are also able to provide more accurate flux density error estimates, whilst avoiding some of the issues associated with the maximum likelihood and LASSO fitting approach used by DESPHOT. In this paper, we show that XID+ outperforms DESPHOT when using just positional information. In Section 2 we discuss the algorithm, and show how the software performs on simulated SPIRE maps in Section 3. In Section 4 we apply XID+ on the HerMES COSMOS SPIRE maps, using a 24 μm catalogue as a prior and show the resulting marginalised SPIRE colour-colour plot and contribution to the cosmic infrared background. We discuss how XID+ can make use of flux prior information, delivered by the HELP project (Hurley et al. in prep) in Section 5 and make final conclusions in 6.

2 XID+ ALGORITHM

The basic goal of XID+ is to use the SPIRE maps to infer the likely SPIRE flux of sources we already know about. Bayesian inference is well suited to these requirements. It allows the use of prior information and provides a posterior distribution of the parameter(s) after taking into account the observed data.

We also want to provide a framework to do science directly with the maps rather than adding the additional step of first creating catalogues, which in essence is a form of lossy data compression.

We therefore adopt a Bayesian probabilistic modelling approach for our XID+ algorithm. It aims to:

- map out the posterior rather than the traditional maximum likelihood point estimate, thereby providing a full account of the flux uncertainty;
- extend the use of prior information beyond just using positional information about sources.

In the following section, we describe our XID+ algorithm. As this algorithm builds upon knowledge gained from the original XID (a.k.a DESPHOT) algorithm used by HerMES (Roseboom et al. 2010, 2011; Wang et al. 2014), we describe XID+ in the context of how it differs from DESPHOT.

2.1 Basic Model

Our data ($\mathbf{d}$) are maps with $n_1 \times n_2 = M$ pixels. Our model assumes the maps are formed from S known sources, with flux density $\mathbf{f}$ and a background term accounting for unknown sources. The point response function (PRF) tells us the contribution each source makes to each pixel in the map. Our map can therefore be described as follows:

$$\mathbf{d} = \sum_{i=1}^{S} \mathbf{P}\mathbf{f_i} + N(0, \Sigma_{instrumental}) + N(B, \Sigma_{confusion}) \quad (1)$$

where $\mathbf{d}$ is our model of the map, $\mathbf{P}$ is the PRF, f_i is the flux density for source i and two independent noise terms, one for instrumental noise, the other for confusion noise which we model as Gaussian fluctuations about B, a global background.

We can rewrite the above equation in the linear form:

$$\mathbf{d} = \mathbf{A}\mathbf{f} \tag{2}$$

Where $\mathbf{d}$ is flattened ta a vector with M pixels, A is a sparse $M \times S$ matrix giving the contribution each source makes to each pixel.

As instrumental and confusion noise are independent, we can combine the two noise terms into one covariance matrix such that $\mathbf{N_d} = \Sigma_{instrumental} + \Sigma_{confusion}$. If we assume the only correlated noise between pixels is from the PSF acting on confusion noise, then diagonal entries of $\mathbf{N_d}$ is simply $\sigma^2_{inst.} + \sigma^2_{conf.}$), and off diagonal entries given by combining the PSF and $\sigma^2_{conf.}$.

We can now define the likelihood as the Gaussian probability function for the data given the flux densities

$$L = p(\mathbf{d}|\mathbf{f}) \propto |\mathbf{N_d}|^{-1/2} \exp\big\{ -\frac{1}{2}(\mathbf{d} - \mathbf{A}\mathbf{f})^T \mathbf{N_d}^{-1}(\mathbf{d} - \mathbf{A}\mathbf{f})\big\} \tag{3}$$

The maximum likelihood solution to this equation can be found by setting $\chi = (\mathbf{d} - \mathbf{A}\mathbf{f})^T \mathbf{N_d}^{-1}(\mathbf{d} - \mathbf{A}\mathbf{f})$, finding the minimum and rearranging such that:

$$\mathbf{f} = (\mathbf{A^T N_d^{-1} A})^{-1} \mathbf{A^T N_d^{-1} d} \tag{4}$$

Equation 4 can be solved directly, either by brute-force matrix inversion or via other linear methods. As discussed in Roseboom et al. (2010, 2011); Wang et al. (2014), linear approaches ignore prior knowledge that fluxes cannot have negative flux density. They are also incapable of discriminating between real and spurious soltuions, which can result in overfitting. To overcome these issues, Roseboom et al. (2011) used the non-negative weighted LASSO algorithm (Tibshirani 1996; Zou 2006; ter Braak et al. 2010).

LASSO is a shrinkage and selection method for linear regression and works by treating sources either as 'inactive' with flux density set to zero, or 'active'. It switches sources on one at a time, with the order determined by reduction in chi-squared gained by turning them on. The process continues until some tolerance is reached.

For XID+, we want to map out the entire posterior, $p(\mathbf{f}|\mathbf{d})$, rather than find the maximum likelihood solution. This has the benefit that it gives us more complete information on how certain we are about the predicted fluxes. The posterior can be defined as:

$$p(\mathbf{f}|\mathbf{d}) \propto p(\mathbf{d}|\mathbf{f}) \times p(\mathbf{f}) \tag{5}$$

where $p(\mathbf{d}|\mathbf{f})$ is our likelihood, defined in equation 3 and $p(\mathbf{f})$ is our prior on the fluxes.

In our probabilistic framework, we can illustrate our model for the map, defined in equation 2 via a probabilistic graphical model (PGM). Figure 1 shows a plate diagram (Bishop 2006) for our PGM of the basic XID+ model, where boxes indicate repeated values such as source (i), pixel (j) and band (λ). Open circles correspond to random variables and dots are deterministic (or fixed) variables, with their relative positions in the boxes indicating what indices they repeat over. For our simplest model, the positional vector

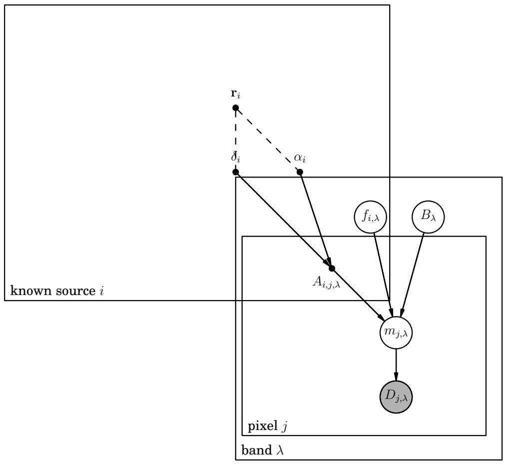

Figure 1. Our probabilistic model for XID+. Boxes represent repeated dimensions, open circles as variables, dots as deterministic (or fixed) variables. Created with DAFT (`http://daft-pgm.org/`)

of sources ($\mathbf{r_i}$) can be described by sky co-ordinates, α_i and δ_i and are treated as deterministic (i.e. known). The PRF is assumed to be a Gaussian, with full-width half-maximum (FWHM) of 18.15, 25.15 and 36.3 arcsec for 250, 350 and 500 μm respectively (Griffin et al. 2010). Both these deterministic variables are used to make the pointing matrix $A_{i,j,\lambda}$ which gives the contribution source i makes to each pixel j in the map at wavelength λ. Each source has its own flux $f_{i,\lambda}$ which is a random variable. By multiplying f, A for all sources and pixels, and adding our global estimate for the background B, we can make our model for the map, m, which we can compare to the data D.

2.1.1 Stan

Now that we have our probabilistic model, we need to sample from it to obtain the posterior. We use the Bayesian inference tool, *Stan*, which is 'a probabilistic programming language implementing full Bayesian statistical inference with MCMC sampling'. *Stan* uses the adaptive Hamiltonian Monte Carlo (HMC) No-U-Turn Sampler (NUTS) of Hoffman & Gelman (2014) to efficiently sample from the posterior. It does this by using the gradient information, allowing fast traversing of high dimensional and highly correlated joint posterior distributions.

Stan has its own modelling language, in which one constructs probabilistic models. Our model for *Stan* can be found in Appendix A.

2.1.2 Estimating Convergence

As with all MCMC routines, one needs to run enough chains and run them long enough to be confident the global minimum has been found and that it has been thoroughly sampled.

As default, we run four separate chains from different initial positions in parameter space. We also discard the first half of the chain as 'warm up' to ensure the chains have converged to the posterior distribution. We then assess the convergence of each parameter by comparing the variation between and within chains using the diagnostics described in Gelman et al. (2013) which can be summarised as follows: Each chain is split in two and the between-chain (BC) and within-chain (WC) variance is calculated. BC and WC are then used to calculate the marginal posterior variance. This in turn can be used to estimate the potential scale reduction $\hat{R}$, which reduces to 1 as the number of iterations tends to infinity. An $\hat{R}$ value > 1.2 suggests chains require more samples. We provide $\hat{R}$ for each parameter.

Due to the nature of MCMC, samples from MCMC routines are correlated. Inference from correlated samples is less precise than from the same number of independent draws. In order to check there are enough independent draws we estimate the effective number of samples $\hat{n_{eff}}$, defined in Gelman et al. (2013). We require $\hat{n_{eff}}$ to be 10 times the number of chains and provide the estimate for each parameter.

2.2 Map segmentation

The survey fields in HELP vary in size from 0.3 to 290 square degrees. Ideally, source photometry and background estimation would be done on the full image. In practice this will be computationally unfeasible. DESPHOT segmented the map by locating islands of high SNR pixels enclosed by low SNR pixels.

We adopt a simpler tiling scheme that splits map data into equal area diamonds based on the Hierarchical Equal Area isoLatitude Pixelization of a sphere (HEALPix). The resolution of the pixels are determined by the HEALPix level, with default for XID+ set at 11 which corresponds to $\approx 1.718'$. When fitting each tile, the perimeter being fitted is extended by one HEALPix pixel with a resolution which is 2 levels higher (i.e. default is level 12 with a resolution of $\approx 25.77'$) such that all sources that could foreseeably contribute to sources within the HEALPix pixel of interest are taken into account.

The choice of HEALPix pixel size affects the computational time of XID+. The required CPU time is found to scale linearly with the amount of data (i.e. number of image pixels). Figure 2 shows the CPU time as a function of image pixel area.

2.3 Uncertainties and Covariances

DESPHOT provides an estimate of the covariance matrix associated with the fluxes ($\mathbf{N_f}$) from $(\mathbf{A^T N_d^{-1} A})^{-1}$. Due to the Cramer-Rao inequality, this estimate is a lower limit. It also assumes the DESPHOT algorithm is linear, which is not strictly true having introduced LASSO and non-negative priors. As a result, the uncertainties are unreliable. For XID+, we have the full posterior, allowing the true variance to be properly characterised. This not only gives us a better estimate for marginalised uncertainty for each source, but it also provides the covariance information between sources (as seen in Figure 7).

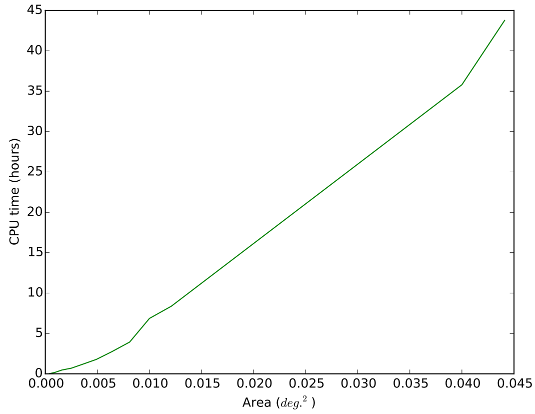

Figure 2. CPU time as a function of tile area (in degrees) for XID+.

3 SIMULATIONS

In order to test and quantify the performance of XID+, we use simulated SPIRE maps of the COSMOS field, a good example of a deep map i.e. where confusion noise ($\sigma_{conf.}$) is much larger than instrumental noise ($\sigma_{inst.}$). In order to get realistic clustering, we use the mock catalogues from the latest version of the Durham semi-analytic model, *GALFORM* (Lacey et al. 2015; Cowley et al. 2015). The model is designed to populate Millennium-class, dark matter only, N-body simulations with a WMAP7 cosmology and minimum halo mass of $1.9 \times 10^{10} h^{-1} M_{\odot}$. The dust model is motivated by the radiative transfer code GRASIL (Silva et al. 1998) and can accurately reproduce the predictions for rest-frame wavelengths $\lambda_{rest} > 70\mu$m.

A mock 100 μm input catalogue, similar to what would be expected of a PACS catalogue, is generated by taking the mock catalogue and making a cut at a flux limit of 50 μJy, giving a total of 64,719 sources over 3.4 square degrees. We use this as our prior input catalogue for both XID+ and DESPHOT. In order to compare performance, we look at three measures: precision, flux accuracy, and flux uncertainty accuracy. For XID+, we only consider sources whose output median flux is above 1 mJy. Likewise, with DESPHOT, we only consider sources which have a maximum likelihood flux of greater than 1 mJy.

3.1 Flux Precision

Precision is a measure of how well the flux is believed to be constrained. For our posterior sample, this relates to the spread of the sample and so we use the interquartile range (75th - 25th percentile; IQR) as our measure of precision. Figure 3 shows the 16th, 50th and 84th percentile (i.e. median and median $\pm\sigma$) of the IQR for 6 bins in true flux. IQR is normalised as a function of input flux for both XID+ and DESPHOT. As one would expect, IQR/S_{True} decreases as a function of input flux, indicating a higher

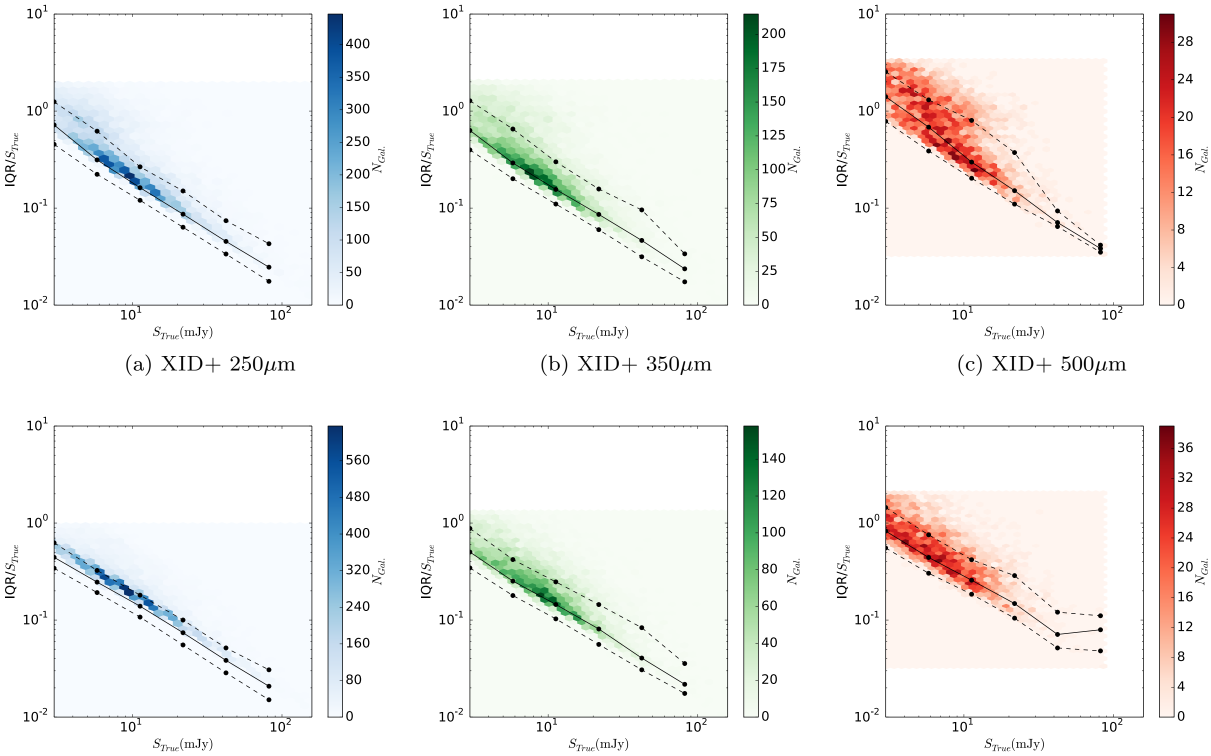

(a) XID+ 250μm (b) XID+ 350μm (c) XID+ 500μm

(d) DESPHOT 250μm (e) DESPHOT 350μm (f) DESPHOT 500μm

Figure 3. Inverse precision, or IQR of XID+ (top) and DESPHOT (bottom) as a function of true flux, for the 250 (blue), 350 (green) and 500 (red) μm SPIRE bands. Black solid and dashed lines shows median and standard deviation respectively. Density of objects is illustrated via underlying colour.

precision is achieved for the brighter sources. While 250 and 350μm outputs achieve a similar level of precision, the outputs for 500μm do not reach the same level of precision. In comparison to DESPHOT, XID+ is marginally less precise for all three bands, though as we show later, DESPHOTs smaller precision comes at a price of severely underestimating uncertianty.

3.2 Flux Accuracy

Flux accuracy is a measure of how far away the estimated flux is from the truth. We use the difference between the median flux estimate from our posterior and the true flux from the simulation, normalised by true flux, as our estimate of flux accuracy. Figure 4 shows how flux accuracy changes as a function of input flux for all three bands. As before, we show the 16th, 50th, and 84th percentile for 6 bins in true flux. For 250 μm, XID+ there is no discernible offset from the truth by $\approx$ 5mJy, whereas DESPHOT underestimates the flux for all but the very brightest sources. For 350 μm and 500 μm, the offset from the truth reaches zero by $\approx$ 10mJy, where as DESPHOT continues to underestimate for all but the very brightest sources.

3.3 Flux Uncertainty accuracy

Estimated flux values should be within one sigma of the true value 68.27% of the time and within 2 sigma 95.45% of the time. We can quantify how many sigma away the true value is from the median in terms of a Z score. A Z score of 1 corresponding to being 1 sigma above the median. Figure 5 shows the flux uncertainty accuracy (or Z score) as a function of input flux. For DESPHOT, uncertainties are assumed to have a normal distribution, truncated at zero. With XID+, we have the full posterior and do not have to make an assumption on the shape of the uncertainty distribution. If we assume the posterior has good frequentist coverage, then we can calculate uncertainty accuracy by taking the percentile at which the true flux value falls within the posterior, and convert the percentile to a corresponding sigma level.

For the 250 μm band, and sources $\lessapprox$ 25mJy, XID+ produces a Z score distribution that matches that expected if uncertainties are correctly estimated (i.e. distribution is centred around zero, with width $\approx$ 1). Above 25mJy, the median Z score increases, indicating that flux uncertainties are being under estimated. In comparison, for all fluxes, the uncertainty distribution from DESPHOT are above 1 and increases to over 2 for the brighter sources. There are also a large number of sources with a Z score greater than 3 (as seen by the higher density in bins at a Z score of 3). This indicates that DESPHOT is a poor estimator with the majority of sources in DESPHOT lying more than 1 σ away from their true flux. The flux uncertainty accuracies for 350 μm and 500 μm show a similar behaviour, though not as severe.

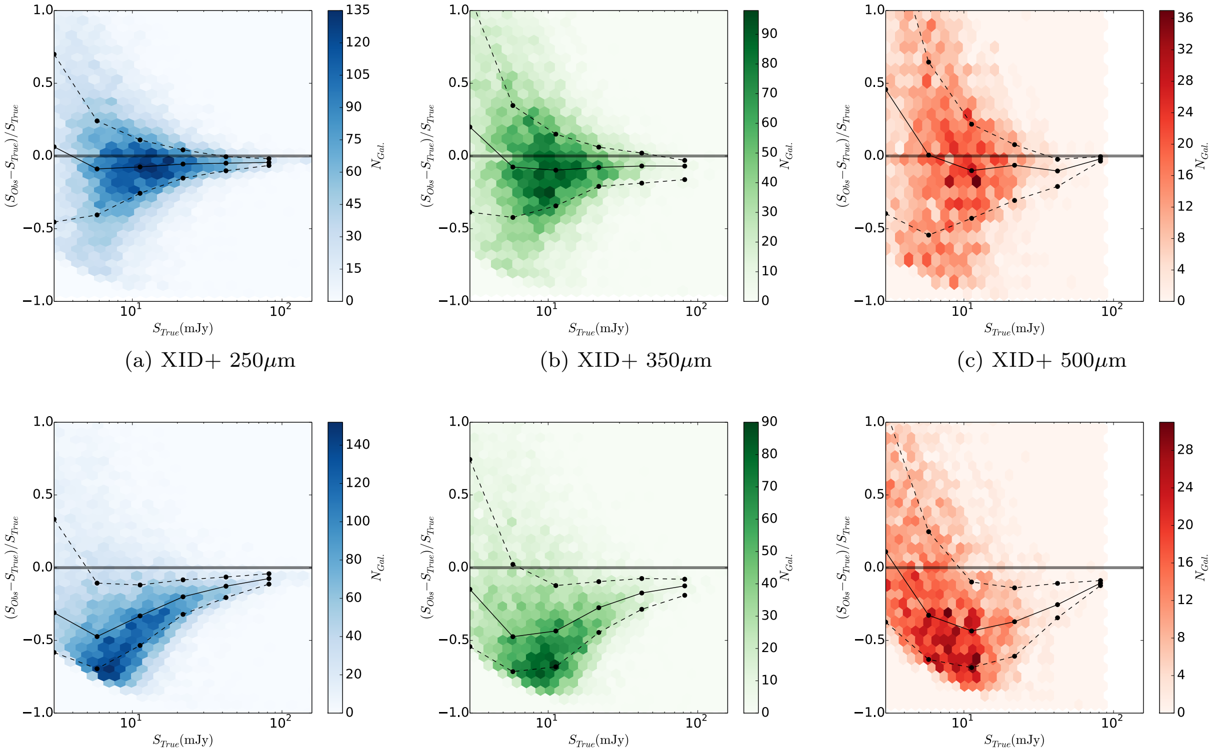

(a) XID+ 250μm (b) XID+ 350μm (c) XID+ 500μm

(d) DESPHOT 250μm (e) DESPHOT 350μm (f) DESPHOT 500μm

Figure 4. Accuracy of XID+ (top) and DESPHOT (bottom) as a function of true flux, for the 250 (blue), 350 (green) and 500 (red) μm SPIRE bands. Black solid and dashed lines shows median and standard deviation respectively. Density of objects is illustrated via underlying colour.

3.4 Convergence

As described in Section 2.1.2, we provide $\hat{R}$ as an estimate of convergence and $\hat{n_{eff}}$ as a measure of independence within the sample. Figures 6 show the histogram for $\hat{R}$ and $\hat{n_{eff}}$ for the three bands, with our thresholds for the statistics shown by dotted lines. In our fit to the simulated SPIRE maps, we use four chains, each with 1500 iterations (half of which are discarded as warm up). This leads to over 99.99% of the sources having an $\hat{R}$ and $\hat{n_{eff}}$ within the threshold for all three bands, indicating our solution is well converged. In cases where convergence has not been reached, the number of iterations can be increased.

3.5 Remaining Noise

The purpose of using prior based source extraction is to overcome the confusion noise in the SPIRE maps, which, as measured by Nguyen et al. (2010) is 5.8, 6.3 and 6.8 mJy at 250, 350 and 500 μm, respectively. By looking at the residual map (i.e. $\mathbf{d}-(\mathbf{Af}+B)$), we can estimate the remaining residual confusion noise in the maps.

We do this by measuring the standard deviation of the pixels in the residual map, convolved with the PRF [1]. This provides an estimate of the total noise remaining in the residual map ($\sigma_{tot.}$). In order to obtain an estimate of the confusion noise ($\sigma_{conf.}$), an estimate of the instrumental noise is made from the uncertainty map, and then removed in quadrature, such that $\sigma^2_{conf.} = \sigma^2_{tot.} - \sigma^2_{inst.}$. Table 1 shows the total and confusion noise from the residual Lacey simulated maps, for both DESPHOT and XID+, and for all three SPIRE bands. For XID+, we calculate a residual map (and remaining noise estimate) for each sample in the posterior, Table 1 shows the median from the sample.

	250μm		350μm		500μm	
	$\sigma_{tot.}$	$\sigma_{conf.}$	$\sigma_{tot.}$	$\sigma_{conf.}$	$\sigma_{tot.}$	$\sigma_{conf.}$
XID+	1.9	1.3	2.2	1.9	2.6	1.9
DESPHOT	2.4	1.9	3.5	3.3	3.4	2.9

Table 1. Table showing the remaining total and confusion noise for the three SPIRE bands (in mJy), from running XID+ and DESPHOT on the Lacey simulated COSMOS maps.

As demonstrated by the values in Table 1, XID+ reaches a confusion noise level substantially lower than that present in the maps. It is also lower than that achieved by DESPHOT. This could be due to the fact we fit the background simultaneously with the sources and/or the LASSO algorithm in DESPHOT restricting the fit of close-by sources, hence increasing the flux variations in the residual map.

[1] The best way to find point sources in a noisy map is to convolve with the PRF, as described in Chapin et al. (2011)

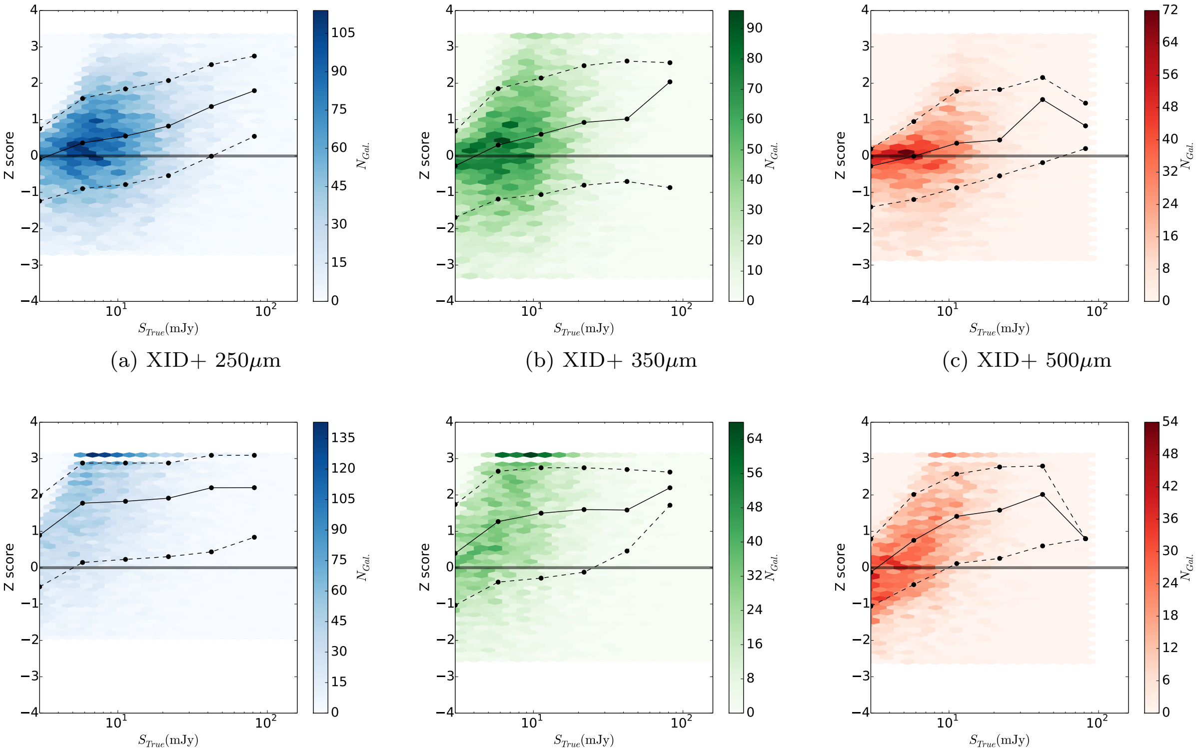

(a) XID+ 250μm (b) XID+ 350μm (c) XID+ 500μm

(d) DESPHOT 250μm (e) DESPHOT 350μm (f) DESPHOT 500μm

Figure 5. Z score, or flux density error for XID+ (top) and DESPHOT (bottom) as a function of true flux, for the 250 (blue), 350 (green) and 500 (red) μm SPIRE bands. Black solid and dashed lines shows median and standard deviation respectively. Density of objects is illustrated via underlying colour.

3.6 Correlated Sources

For sources that are close together (i.e. within FWHM of the PRF), the uncertainty on the flux estimates can be correlated. One of the advantages of obtaining the full posterior is that we get a proper estimate of uncertainty and its correlation. This is particularly apparent when comparing flux estimates with DESPHOT, which, by using the LASSO algorithm forces one source to have all the flux and the other nearby source to zero. Figure 7 shows an example of two sources which are 2" apart. The 250 μm flux estimate from both XID+ and DESPHOT are shown in green and blue respectively. The posterior provided by XID+, fully captures the correlated uncertainty, where as the 'winner takes all' approach from DESPHOT clearly fails to estimate the true flux for both sources.

4 COSMOS FIELD

Having satisfactorily demonstrated the performance on simulations, we have run XID+ on the HerMES COSMOS SPIRE maps from the 2nd Data release. As a prior, we take the MIPS 24 μm catalogue (Floc'h et al. 2009), which covers an area of 2.265 square degrees and includes 52,092 sources with a 24 μm flux density above 60 μJy, which corresponds to a signal to noise cut of 3. Figure 8 shows the marginalised probability density of our MIPS 24 μm prior catalogue in SPIRE colour-colour space and is constructed by combining the 1500 samples from the posterior, for all 52,092 sources. The redshift tracks for Arp220 and M82 (Polletta et al. 2007) are over-plotted and run through the highest density region at redshifts of around 2-3. Figure 9 shows the cumulative contribution to the cosmic infrared background (CIRB) at 250, 350 and 500 μm from our MIPS 24 μm prior catalogue, as a function of 24 μm flux. The filled bands illustrate the FIRAS absolute measurements from Lagache & Puget (2000), while dashed and dashed dotted lines indicate the contribution to the CIRB from SPIRE resolved sources (Oliver et al. 2010). By going to a depth of 60 μJy in the 24 μm catalogue, we reach 5.573 ± 0.003, 2.805 ± 0.002 and 1.24 ± 0.002 nWm^{-2}sr^{-1} or 47, 44 and 46% of the nominal measured values at 250, 350 and 500 μm (Lagache & Puget 2000). As a comparison, at the (40 beams)$^{-1}$ depth, (Oliver et al. 2010) resolve 1.73 ± 0.33, 0.63 ± 0.18, 0.15 ± 0.07 or 15, 10, 6%.

Our final data product consists of a catalogue, summarising the SPIRE fluxes via the 16th, 50th and 84th percentile (i.e. median and median $\pm\sigma$), the median background and the convergence statistics. We also make available the 3000 samples from the posterior probability distribution, each of which can be thought of as a possible catalogue in probability space.

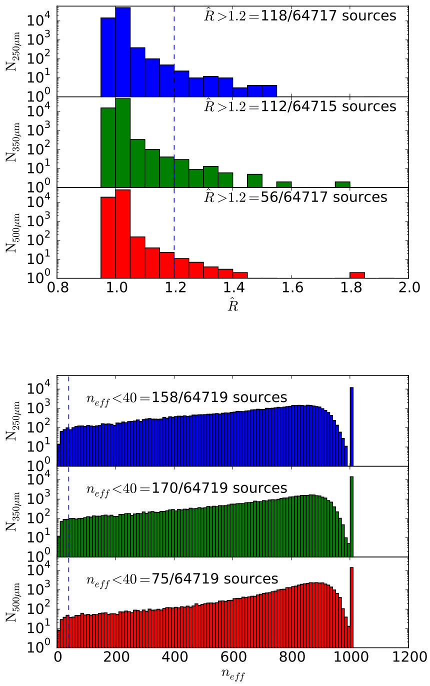

Figure 6. $\hat{R}$ and $\hat{n_{eff}}$ values for all sources fitted in the simulation. The majority of sources have converged and have enough effective samples.

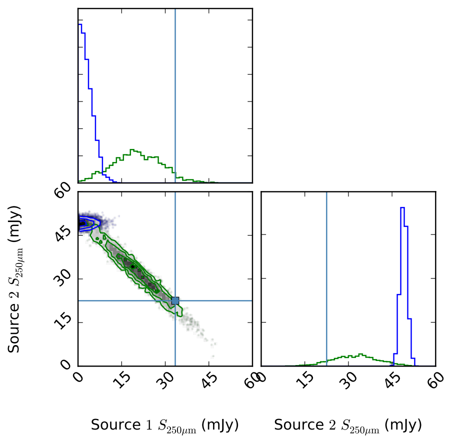

Figure 7. Posterior triangle plot of two correlated sources that are 2" apart, with one and two sigma contours over-plotted and true fluxes indicated via the vertical and horizontal line. DESPHOT (blue) assigns all the flux to one source, where as with XID+ we get the full uncertainty information from the posterior. Plot created with Foreman-Mackey et al. (2014).

5 DISCUSSION

We have run XID+ on simulated maps of the COSMOS field and compared it to DESPHOT using three main metrics; flux accuracy, precision and uncertainty accuracy. On accuracy, XID+ performs significantly better in all three bands, and although appearing marginally less precise, the loss of precision relates to more realistic estimates for flux uncertainties.

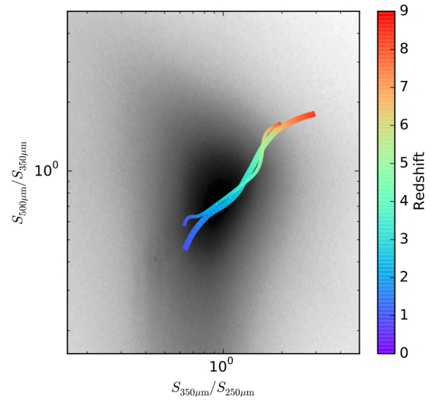

Figure 8. The marginalised SPIRE colour-colour probability density (in black) from the MIPS 24 μm sources. Over plotted are the redshifted spectral energy distributions for Arp220 (thick line) and M82 (thin line)(Polletta et al. 2007).

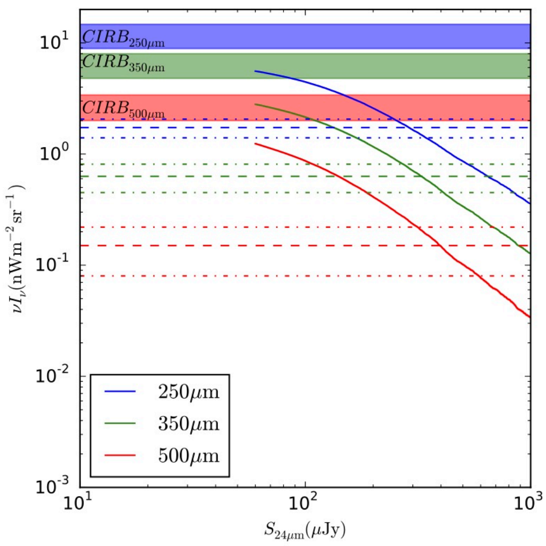

Figure 9. The cumulative contribution to the cosmic infrared background (CIRB) from our MIPS 24 μm sources, as a function of 24 μm flux, at 250 (blue), 350 (green) and 500 (red) μm. The one σ confidence regions for the CIRB at SPIRE wavelengths, as measured by Lagache & Puget (2000) are plotted with blue, green and red bands. The mean and one σ uncertainty for the CIRB resolved by SPIRE (Oliver et al. 2010) are shown with dashed and dashed-dotted lines.

The higher performance gained by XID+ comes from fully capturing the posterior probability distribution on flux estimates. By exploring the posterior, we get a proper handle on uncertainties and no longer have to employ penalisation techniques such as LASSO, which are known to behave erratically.

By using a probabilistic approach, we have a framework where we can introduce prior information on the source fluxes in a transparent manner. For this basic version, we use a simple $\log_{10}$ uniform prior, with bounds at 10^{-2} and 10^{3}mJy. However, as can be seen in Figure 7, where sources are correlated, if we have prior knowledge on the flux of one of the sources, it can help us determine a more precise flux for the other.

As demonstrated by Safarzadeh et al. (2015), these priors could come from fitting spectral energy distribution models to multi-wavelength ancillary data. Another alternative is to use machine-learning algorithms to 'learn' the expected flux from the statistical population. As part of HELP, the testing and benchmarking of suitable methods for deriving SPIRE flux priors will be presented in Hurley et al. (in prep).

More generally, the probabilistic model used in XID+ can easily be expanded, allowing distributions such as the flux distribution (or number counts) to be modelled explicitly. In principle, the probabilistic model could become detailed enough to simultaneously fit luminosity functions and the location of locus of the SFR-M* relation at different redshift and we will explore these expansions in future papers.

6 CONCLUSIONS

In this paper we have introduced the prior based source detection software, XID+. By using the Bayesian inference tool *Stan*, we are able to fully sample the posterior probability distribution, which in turn gives a better understanding of the uncertainty associated with the source flux.

Having run XID+ on simulated maps, we have shown this is extremely advantageous for maps that are confusion limited, such as the *Herschel* observations that are part of *HerMES*. In comparison to the current maximum likelihood based software DESPHOT, XID+ performs far better in all three main metrics; flux accuracy, precision and uncertainty accuracy.

We have run XID+ on the HerMES COSMOS SPIRE maps from the 2nd Data release, using the MIPS 24 μm catalogue (Floc'h et al. 2009) as our prior. Using the full posterior, we have created a marginalised SPIRE colour-colour plot, illustrating the probability distribution of our MIPS 24 μm catalogue in SPIRE colour-colour space. We have also shown that the MIPS 24 μm sources contribute 47, 44 and 46% to the cosmic infrared background at 250, 350 and 500 μm. We provide the catalogue and posterior probability distribution samples as a data product at ..... As far as we are aware, this is the first time the full posterior probability distribution is made available as a data product for list driven photometry.

ACKNOWLEDGEMENTS

REFERENCES

Béthermin M., et al., 2012, Astron. Astrophys., 542, A58
Bishop C. M., 2006, Pattern Recognition and Machine Learning. Springer
Chapin E. L., et al., 2011, Monthly Notices of the Royal Astronomical Society, 411, 505
Cowley W. I., Lacey C. G., Baugh C. M., Cole S., 2015, MNRAS, 446, 1784
Eales S., et al., 2010, PASP, 122, 499
Elbaz D., et al., 2010, A&A, 518, L29
Floc'h E. L., et al., 2009, The Astrophysical Journal, 703, 222
Foreman-Mackey D., Price-Whelan A., Ryan G., Emily, Smith M., Barbary K., Hogg D. W., Brewer B. J., 2014, triangle.py v0.1.1
Gelman A., Carlin J., Stern H., Dunson D., Vehtari A., Rubin D., 2013, Bayesian Data Analysis, Third Edition, Chapman & Hall/CRC Texts in Statistical Science. Taylor & Francis
Griffin M. J., et al., 2010, Astron. Astrophys., 518, L3
Hoffman M. D., Gelman A., 2014, Journal of Machine Learning Research, 15, 1593
Holland W. S., et al., 2013, MNRAS, 430, 2513
Holland W. S., et al., 1999, MNRAS, 303, 659
Ivison R. J., et al., 2010, A&A, 518, L31
Kessler M. F., et al., 1996, Astron. Astrophys., 315, L27
Lacey C. G., et al., 2015, ArXiv e-prints
Lagache G., Puget J. L., 2000, Astron. Astrophys., 355, 17
Marsden G., et al., 2009, ApJ, 707, 1729
Murakami H., et al., 2007, PASJ, 59, 369
Neugebauer G., et al., 1984, Astrophysical Journal, 278, L1
Nguyen H. T., et al., 2010, A&A, 518, L5
Oliver S., in prep., Herschel extragalactic legacy project
Oliver S. J., et al., 2012, Monthly Notices of the Royal Astronomical Society, 424, 1614
Oliver S. J., et al., 2010, Astron. Astrophys., 518, L21
Pascale E., et al., 2009, ApJ, 707, 1740
Pilbratt G. L., et al., 2010, Astronomy and Astrophysics, 518, L1
Poglitsch A., et al., 2010, Astron. Astrophys., 518, L2
Polletta M., et al., 2007, Astrophys. J., 663, 81
Puget J.-L., Abergel A., Bernard J.-P., Boulanger F., Burton W. B., Desert F.-X., Hartmann D., 1996, Astron. Astrophys., 308, L5
Roseboom I. G., et al., 2011, Monthly Notices of the Royal Astronomical Society, 419, 2758
Roseboom I. G., et al., 2010, arXiv
Safarzadeh M., Ferguson H. C., Lu Y., Inami H., Somerville R. S., 2015, Astrophys. J., 798, 91
Silva L., Granato G. L., Bressan A., Danese L., 1998, Astrophys. J., 509, 103
Soifer B. T., et al., 1984, Astrophysical Journal, 278, L71
Stan Development Team, 2015a, Pystan: the python interface to stan, version 2.7.0
Stan Development Team, 2015b, Stan: A c++ library for probability and sampling, version 2.7.0
ter Braak C. J., Boer M. P., Totir L. R., Winkler C. R., Smith O. S., Bink M. C., 2010, Genetics, 185, 1045
Tibshirani R., 1996, Journal of the Royal Statistical Society (Series B), 58, 267
Wang L., et al., 2014, Monthly Notices of the Royal Astronomical Society, 444, 2870
Werner M. W., et al., 2004, The Astrophysical Journal Supplement Series, 154, 1
Wright E. L., et al., 2010, AJ, 140, 1868
Zou H., 2006, Journal of the American Statistical Association, 101, 1418

APPENDIX A

```
//Full Bayesian inference fit  XID
data {
  int<lower=0> nsrc;//number of sources
  //-----PSW-----
  int<lower=0> npix_psw;//number of pixels
  int<lower=0> nnz_psw; //number of non neg entries in A
  vector[npix_psw] db_psw;//flattened map
  vector[npix_psw] sigma_psw;//flattened uncertianty map (assuming no covariance between pixels)
  real bkg_prior_psw;//prior estimate of background
  real bkg_prior_sig_psw;//sigma of prior estimate of background
  vector[nnz_psw] Val_psw;//non neg values in image matrix
  int Row_psw[nnz_psw];//Rows of non neg valies in image matrix
  int Col_psw[nnz_psw];//Cols of non neg values in image matrix
  //-----PMW-----
  int<lower=0> npix_pmw;//number of pixels
  int<lower=0> nnz_pmw; //number of non neg entries in A
  vector[npix_pmw] db_pmw;//flattened map
  vector[npix_pmw] sigma_pmw;//flattened uncertianty map (assuming no covariance between pixels)
  real bkg_prior_pmw;//prior estimate of background
  real bkg_prior_sig_pmw;//sigma of prior estimate of background
  vector[nnz_pmw] Val_pmw;//non neg values in image matrix
  int Row_pmw[nnz_pmw];//Rows of non neg valies in image matrix
  int Col_pmw[nnz_pmw];//Cols of non neg values in image matrix
  //-----PLW-----
  int<lower=0> npix_plw;//number of pixels
  int<lower=0> nnz_plw; //number of non neg entries in A
  vector[npix_plw] db_plw;//flattened map
  vector[npix_plw] sigma_plw;//flattened uncertianty map (assuming no covariance between pixels)
  real bkg_prior_plw;//prior estimate of background
  real bkg_prior_sig_plw;//sigma of prior estimate of background
  vector[nnz_plw] Val_plw;//non neg values in image matrix
  int Row_plw[nnz_plw];//Rows of non neg valies in image matrix
  int Col_plw[nnz_plw];//Cols of non neg values in image matrix

}
parameters {
  vector<lower=-2.0,upper=3.0> [nsrc] src_f_psw;//source vector
  real bkg_psw;//background
  vector<lower=-2.0,upper=3.0> [nsrc] src_f_pmw;//source vector
  real bkg_pmw;//background
  vector<lower=-2.0,upper=3.0> [nsrc] src_f_plw;//source vector
  real bkg_plw;//background

}


model {
  vector[npix_psw] db_hat_psw;//model of map
  vector[npix_pmw] db_hat_pmw;//model of map
  vector[npix_plw] db_hat_plw;//model of map


  vector[nsrc+1] f_vec_psw;//vector of source fluxes and background
  vector[nsrc+1] f_vec_pmw;//vector of source fluxes and background
  vector[nsrc+1] f_vec_plw;//vector of source fluxes and background


  //Prior on background
  bkg_psw ~normal(bkg_prior_psw,bkg_prior_sig_psw);
  bkg_pmw ~normal(bkg_prior_pmw,bkg_prior_sig_pmw);
  bkg_plw ~normal(bkg_prior_plw,bkg_prior_sig_plw);
```

```
  //Prior on flux of sources (not being used yet)
  //src_f_psw ~normal(-1,2.2);
  //src_f_pmw ~normal(-1,2.2);
  //src_f_plw ~normal(-1,2.2);


  //background is now contribution from confusion only!!
  f_vec_psw[nsrc+1] <-bkg_psw;
  f_vec_pmw[nsrc+1] <-bkg_pmw;
  f_vec_plw[nsrc+1] <-bkg_plw;

  // Transform to normal space. As I am sampling variable then transforming I don't need a Jacobian
  for (n in 1:nsrc) {
    f_vec_psw[n] <- pow(10.0,src_f_psw[n]);
    f_vec_pmw[n] <- pow(10.0,src_f_pmw[n]);
    f_vec_plw[n] <- pow(10.0,src_f_plw[n]);


  }


  // Create model maps (i.e. db_hat = A*f) using sparse multiplication
  for (k in 1:npix_psw) {
    db_hat_psw[k] <- 0;
  }
  for (k in 1:nnz_psw) {
    db_hat_psw[Row_psw[k]+1] <- db_hat_psw[Row_psw[k]+1] + Val_psw[k]*f_vec_psw[Col_psw[k]+1];
      }

  for (k in 1:npix_pmw) {
    db_hat_pmw[k] <- 0;
  }
  for (k in 1:nnz_pmw) {
    db_hat_pmw[Row_pmw[k]+1] <- db_hat_pmw[Row_pmw[k]+1] + Val_pmw[k]*f_vec_pmw[Col_pmw[k]+1];
      }

  for (k in 1:npix_plw) {
    db_hat_plw[k] <- 0;
  }
  for (k in 1:nnz_plw) {
    db_hat_plw[Row_plw[k]+1] <- db_hat_plw[Row_plw[k]+1] + Val_plw[k]*f_vec_plw[Col_plw[k]+1];
      }



  // likelihood of observed map|model map
  db_psw ~ normal(db_hat_psw,sigma_psw);
  db_pmw ~ normal(db_hat_pmw,sigma_pmw);
  db_plw ~ normal(db_hat_plw,sigma_plw);
}
```